Insight into the behaviour of bamboo culms subjected to bending

Theodora Mouka,[a], Elias G. Dimitrakopoulos,[a,*], Rodolfo Lorenzo,[b]

[a]Department of Civil and Environmental Engineering,
The Hong Kong University of Science and Technology, Clear Water Bay, Kowloon, Hong Kong, China
[b]Department of Civil, Environmental and Geomatic Engineering,
University College London, Gower Street, London WC1E 6BT, UK

Abstract

This study describes analytically the behaviour of bamboo culms subjected to bending, and predicts the failure load and stiffness loss after the linear-elastic stage. Basis of the failure load prediction is the identification of the critical failure mechanisms. The study examines analytically four distinct failure mechanisms; Brazier instability, longitudinal tension/compression, tension perpendicular to the fibres, and shear parallel to the fibres. It concludes that, for the three bamboo species examined (Moso, Guadua and Kao Jue), critical failure mechanisms are tension perpendicular to the fibres (with potential tension-shear interaction), and longitudinal compression. Which of the two mechanisms occurs first depends on the case-specific material properties and culm radius-to-thickness ratio. Regarding stiffness loss, main cause is longitudinal splitting. The extent of the stiffness loss depends on crack length, crack number, and crack location along the culm circumference. Secondary cause are non-linear geometric effects at the large deflection stage. Assuming a parabolic deformed shape, a single equation can describe the stiffness loss induced by non-linear geometric effects, regardless of material properties and culm geometry. Comparing the analytical results with pertinent experimental data, the proposed equations are sufficiently accurate in their prediction of failure load and stiffness loss, although they tend to underestimate both.

Keywords: Bamboo flexure, Orthotropic tubes, Bending failure, Stiffness loss, Non-linear geometry

1. Introduction

Traditional construction materials, such as concrete and steel, have a significant carbon footprint and are responsible for the majority of the construction sector carbon emissions [1]. In contrast, bamboo is a natural material that has been used in construction around the world, mostly, where it is indigenous. It has high strength-to-weight ratio [2], substantial carbon sequestration capacity [3], and is fast-growing [4]. These remarkable properties render it a potentially sustainable construction material, towards the UN goal for a "zero-emission buildings and construction sector" [5].

The lack of detailed design standards —despite recent progress [6]— and incomplete understanding of bamboo structural member behaviour hinder its wider adoption in construction. Specifically, bamboo is a natural composite with hierarchical structure that governs its mechanical behaviour [7–10]. Full-culm (or round-culm) bamboo flexural members exhibit a particularly complicated mechanical behaviour, which typically entails an initial elastic stage, followed by a stage where stiffness progressively declines, until failure [11–13]. To date, the mechanisms that cause this non-linear stiffness loss are unclear, while recent research [13] indicates that this stiffness loss is not because of material plasticity.

Additionally, bamboo culms display multiple failure modes when subjected to bending [14]. The extensive experimental program of Trujillo et al. [14] of four-point bending tests on full-culm bamboo, identified five failure modes: shear failure (evidenced by a longitudinal crack), culm crushing at the load application points/supports, compression failure, tension failure, and culm collapse. This is particularly problematic, since current bamboo testing standards (e.g. ISO 22157 [15]) specifically mandate that crushing or kinking of the culm wall during the test should be avoided. For example, ISO 22156:2021 [6] includes particular geometric specifications for bamboo culms, to prevent crushing and kinking in culms used in construction. Yet, experimental studies indicate that crushing and kinking are common failure modes [11, 13, 14, 16, 17]. Additionally, full-culm bamboo modulus of rupture (MOR) depends on culm diameter and density [16], further showcasing the complexity of bamboo culm flexure. Hence, the MOR measured in bending tests is not a material property, but rather a property of the structural member. As such, it is case-specific, and cannot be utilised universally in structural design. To alleviate the uncertainties stemming from geometric variability, some studies propose structural grading [14, 17], as basis for a capacity-based approach [14]. Regardless, there is a need to explain the gradual loss of stiffness, that initiates before any apparent failures, and to identify the underlying universal failure mechanisms.

Pertinent analytical investigations, which would shed light on the problem, are scarce. Lorenzo et al [18] showed that a bimodulus approach (different elastic modulus in tension and compression) predicts more accurately the longitudinal stress and strain distributions of bamboo culms in bending. The analytical study of Tian et al [19] adopted the bimodulus model of [18] and assumed an elastic-plastic material law in compression, to simulate the force-displacement curve. Wegst and Ashby [20] studied analytically the potential failure modes of orthotropic tubes subjected to bending, and associated them with shape factor ϕ (radius to thickness ratio). Lorenzo et al [13], using some of the equations of [20] and numerical models, concluded that, for Moso bamboo, circumferential tensile stresses are the most critical to failure. They also showed numerically that the loss of stiffness after the initial linear elastic stage is due to the cracks that open when the circumferential tensile strength is exceeded. Several experimental studies [11, 14, 16, 17] utilised the Euler-Bernoulli beam theory to analyse bending of bamboo culms, thus examining solely longitudinal tension/compression failure.

The present work aims to predict analytically the behaviour and failure modes of bamboo culms subjected to bending. Motivation of the study is resolving the current contradicting findings on failure initiation, thus complementing existing knowledge on full-culm bamboo flexure. Of specific interest are 1) the underlying mechanisms that cause failure and, subsequently, the prediction of the failure load and 2) the reasons behind the gradual loss of stiffness after the initial linear-elastic stage. As a reference, and to verify the analytical results, we use available experimental results [11, 13, 14, 21]. The goal is to contribute to the design of bamboo flexural members, by bringing forward the salient physical mechanisms that govern the flexure of bamboo.

2. Experimental behaviour

This study aims to predict experimental results on bamboo flexure [11, 13, 14, 21] analytically. As an example, consider the experimental force-displacement curve of a typical Moso (*Phyllostachys pubescens*) bamboo culm (specimen ML3 [13]) subjected to four-point bending according to [15] (figure 1). The culm has an average external diameter of 99 mm and a thickness of 9 mm. The flexural modulus of elasticity, calculated from the experimental data, is 12320 MPa [13]. At the supports and at the load application points, the culm is in contact with wooden saddles with a 90° notch (figure 1b). The reference experimental curve (figure 1c) has an initial linear stage, up to approximately 60% of the ultimate load. After the linear stage, the stiffness (slope of the curve) gradually drops, until it becomes almost zero at
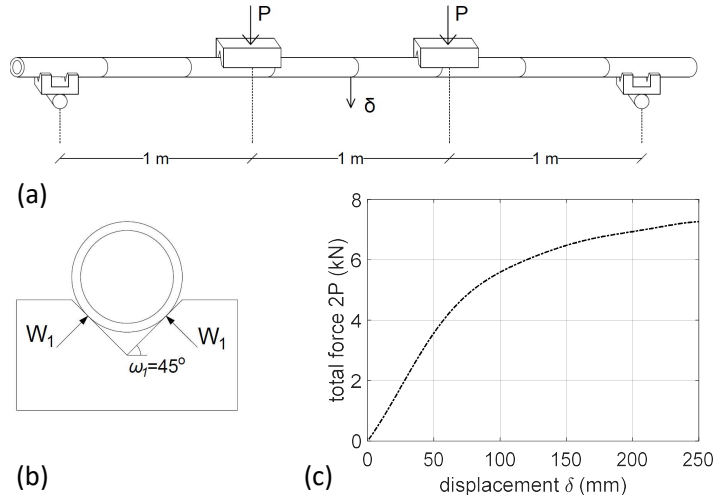
Figure 1: (a) Schematic representation of the four-point bending test of [13], (b) Schematic representation of saddle support profile, (c) Experimental force-displacement curve of a typical Moso bamboo culm [13].

the ultimate load. Note that 'clicking' sounds were observed after the linear stage, but otherwise no visible failure, until the ultimate load [13]. That study [13] also proved numerically that the loss of stiffness originates in the longitudinal cracks that appear at the areas where the circumferential tensile strength is exceeded. At the ultimate load, the culm fails catastrophically by longitudinal splitting at the four quadrants of the cross-section.

3. Failure mechanisms

Bamboo culms under flexure can fail in various ways. Wegst and Ashby [20] identify three failure mechanisms for orthotropic tubes. The first one has to do with the instability caused by ovalisation of the cross-section, which causes local kinking of the culm (Brazier effect [22]). This happens when the bending moment reaches a critical value, the so-called Brazier moment. The second failure mechanism is due to the longitudinal stresses, either on the tension or on the compression side, depending on which strength (tensile/compressive) is lower. The last failure mode is longitudinal splitting, but there is controversy on the mechanism that causes it. Some studies [13, 20, 23, 24] attribute it to circumferential tension, since the circumferential tensile strength of bamboo is low. Others argue that the main cause is shear, or the interaction between shear and circumferential tension [14, 25].

This section examines analytically the different potential failure modes. The goal is to determine which is most likely to occur, taking into account culm geometry. To that end, we determine the critical bending moments for each of the failure mechanisms, and create a failure map (similar to the one in [20]) of the critical bending moment as a function of the shape factor ϕ of the culm:

$$\phi = \frac{R}{t} \tag{1}$$

where R is the culm (midline) radius and t is the culm thickness. Shape factor ϕ relates to the more commonly used for bamboo ratio of external diameter D to thickness t as:

$$\frac{D}{t} = 2\phi + 1 \tag{2}$$

The calculations of this section ignore any favourable effect the nodes might have on cross-section ovalisation. We do not expect this to be far from reality, since, given the high anisotropy of bamboo, the required internode length for effective
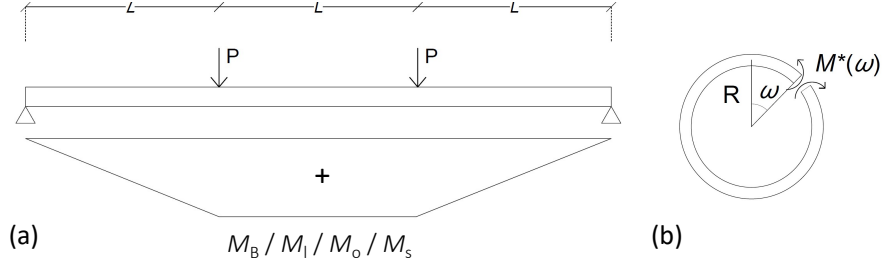
3

Figure 2: Bending moment notation

ovalisation mitigation is far shorter than typical bamboo internode lengths (preliminary calculations according to [20] point to a required internode length of 0.2∼0.3 culm diameters, which is impractical). Thus, ovalisation in bamboo cannot be prevented (which is in agreement with [20]), and, according to preliminary calculations, the failure of bamboo culms is similar to that of infinitely long tubes without stiffeners. Moreover, the calculations herein do not directly consider the property gradient along the culm wall thickness, which improves the culm's mechanical efficiency, as it is optimised for the loads bamboo as a plant needs to carry during its lifespan [26, 27]. This study accounts indirectly for the property gradient's effect on the culm's mechanical properties, by adopting "apparent" Young's modulus values, determined by edge-bearing (or similar) tests for the circumferential direction and by culm bending tests for the longitudinal direction. Therefore, the adopted values are "effective" values, and hence by definition replicate the macroscopic behaviour (flexural behaviour of the culm wall in the plane of the cross-section, and of the tubular culm in the longitudinal direction).

Thus, for the first two failure mechanisms, we adopt the equations of [20]. Hence, the critical bending moment for ovalisation-induced failure (Brazier moment [22], M_B, figure 2a) of an orthotropic tube is [20]:

$$\frac{M_B}{A^{1.5}} = \frac{1}{9\sqrt{\pi}}\sqrt{\frac{E_\parallel E_\perp}{\phi}} \tag{3}$$

where A is the cross-section area, ϕ is the shape factor (equation (1)), $E_\parallel$ is the longitudinal Young's modulus and $E_\perp$ is the transverse (circumferential) Young's modulus. Respectively, the critical bending moment for tensile/compressive failure in the longitudinal direction (M_l, figure 2a) is [20]:

$$\frac{M_l}{A^{1.5}} = \frac{1}{\sqrt{8\pi}}\sigma_{u\parallel}\sqrt{\phi} \tag{4}$$

where $\sigma_{u\parallel}$ is the axial tensile or compressive strength, whichever is lower.

3.1. Splitting induced by circumferential tension

When a bamboo culm is subjected to a bending moment M_o (figure 2a), its cross-section tends to ovalise. During ovalisation, the culm wall bends in the plane of the cross-section, hence circumferential stresses occur. Since the material's transverse tensile strength typically is low, tensile circumferential stresses can cause the culm to split in the longitudinal direction. This happens even at low circumferential strains [2], where cross-section ovalisation is not apparent. This section adopts the methodology of [20] to associate circumferential tensile strength with the bending moment M_o (figure 2a) that caused the ovalisation.

Let M^* be the moment that induces bending of the culm wall (which can be considered as a curved beam) in the plane of the cross-section (figure 2b). The value and position of maximum M^* depend on the assumed loading of the
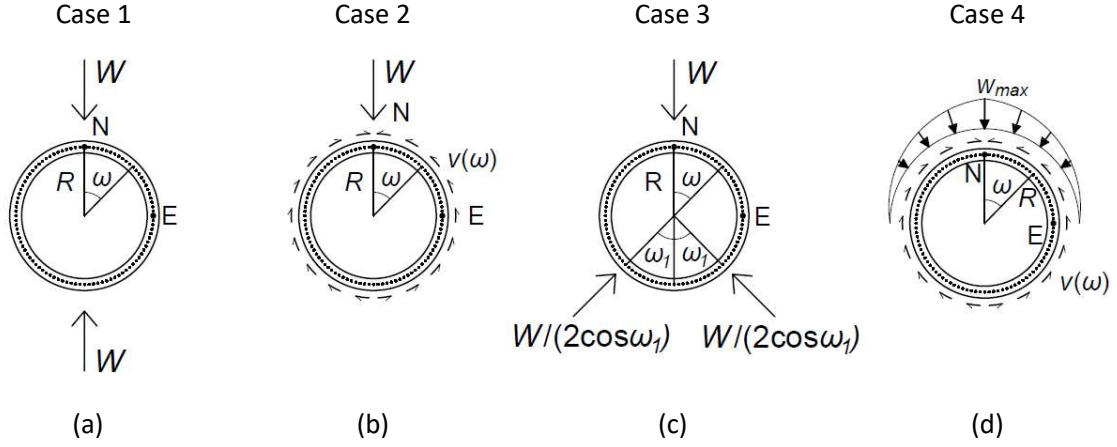
4

Figure 3: Cross-section load cases.

curved beam [28]. The exact loading (external load and internal shear flow) at the critical cross-sections is not easy to determine, and differs from case to case, depending on the experimental setup or, in an actual bamboo structure, on the manner in which loads are transferred to the beams. Study [20] assumes the loading of figure 3a (Case 1) and considers M^* at position E. We investigate three additional load cases (figure 3b-d), and consider the maximum M^*. All cases considered are approximations of actual load cases, and thus are not strictly accurate. Cases 2~4 (figure 3b-d) simulate the state of the cross-section at the loading points and at the supports, which is where the longitudinal splitting typically initiates [13, 14, 25]. Case 2 (figure 3b) assumes a point load W (external load of the cross-section) resisted by a shear flow v in the plane of the cross-section, distributed as:

$$v\left(\omega\right) = \frac{W\sin\omega}{\pi R} \tag{5}$$

This is an approximation, since the actual external load on the cross-section is not a point load, for example if the experiment follows the saddle configuration suggested in [15]. For this reason, we also investigate Case 3 (figure 3c), with two radial loads at $\omega_1 = \pm 45^o$, which represent the loads at the contact points between the saddles and the culm. Finally, the last case (Case 4), involves a radial pressure that varies linearly with angle ω, and its maximum value is w_{max}, at point N (figure 3d). Load W, which is the total applied vertical force, associates with w_{max} as [28]:

$$W = \frac{4w_{\max}R}{\pi} \tag{6}$$

The radial pressure is resisted by a shear flow, similarly to Case 2 (equation 5). Case 4 aims to approximate the support conditions encouraged by current testing standards (e.g., [15]), where the applied load is distributed on as much of the culm circumference as possible (e.g. via straps), and thus is not a point load.

Equations (7)-(10) [28] describe M^* as a function of angle ω ($0 \le \omega \le \pi$) for each of the load cases 1-4 (figure 3):

$$M_1^*\left(\omega\right) = WR\left(\frac{1}{\pi} - \frac{1}{2}\sin\omega\right) \tag{7}$$

$$M_2^*\left(\omega\right) = \frac{WR}{2\pi}\left[1 + \frac{1}{2}\cos\omega - (\pi - \omega)\sin\omega\right] \tag{8}$$
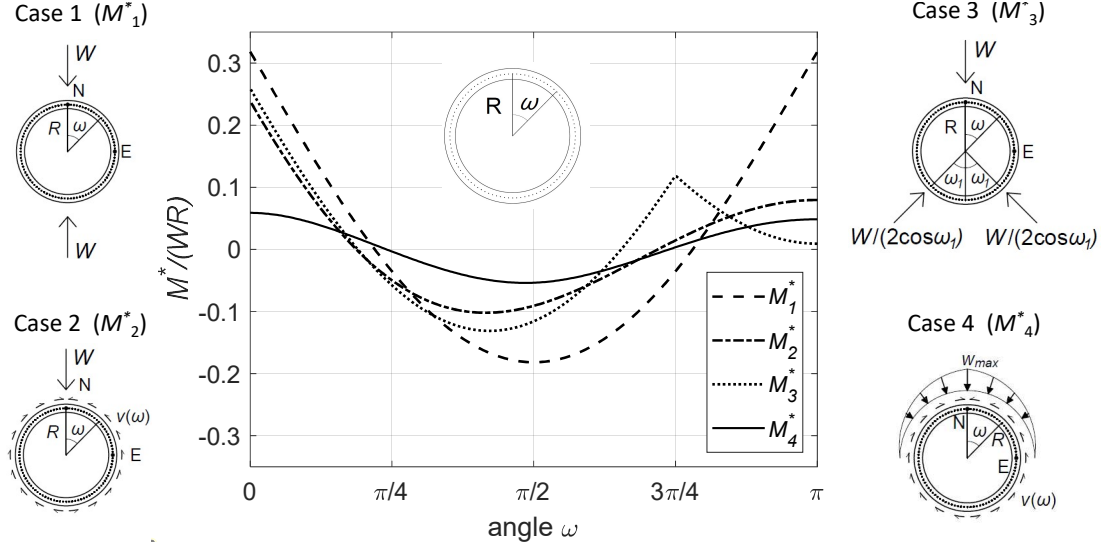
5

Figure 4: Bending moment M^* (normalised with WR) as a function of angle ω for each of the cross-section load cases.

$$M_3^* (\omega) = \begin{cases} \frac{WR}{2} \left[\frac{\sqrt{2}+1}{\pi} + \frac{3}{4} \cos \omega - \sqrt{2} \sin \left(\omega + \frac{\pi}{4} \right) \right], & \omega \leq \frac{3\pi}{4} \\ \frac{WR}{2} \left(\frac{\sqrt{2}+1}{\pi} + \frac{3}{4} \cos \omega \right), & \omega > \frac{3\pi}{4} \end{cases} \tag{9}$$

$$M_4^* (\omega) = \begin{cases} \frac{WR}{2\pi} \left[\left(\frac{5}{2} + \frac{\pi}{2} \right) \cos \omega - (\pi - \omega) \sin \omega + \pi \omega - \frac{3\pi^2}{8} \right], & \omega \leq \frac{\pi}{2} \\ \frac{WR}{2\pi} \left[\left(\frac{5}{2} - \frac{\pi}{2} \right) \cos \omega - (\pi - \omega) \sin \omega + \frac{\pi^2}{8} \right], & \omega > \frac{\pi}{2} \end{cases} \tag{10}$$

M^* is positive when it causes tension at the inner side. Figure 4 shows the effect of cross-section loading (Cases 1 to 4) on the resulting bending moment M^*. For all cases, maximum positive M^* appears under load W ($\omega = 0^o$, figure 3). Maximum negative M^* appears at $\omega \approx 90^o$ in Cases 1 and 4 and at $\omega \approx 75^o$ in Cases 2 and 3. In Case 3, there is an additional potentially critical location; at the saddle contact points ($\omega = 135^o$, figure 4). There, M_3^* is positive and of approximately the same value as the maximum negative M_3^* at $\omega \approx 75^o$. In Case 4, the absolute value of M^* is approximately the same at $\omega = 0^o$ and at $\omega = 90^o$, rendering these locations equally critical. Figure 4 shows that, in the case of a distributed load (Case 4), M^* is significantly less, compared to the point load case (Case 2). Importantly, the sensitivity of M^* to the applied load distribution highlights the significance of the manner in which loads are applied on the culms for culm failure, thus having implications for testing standards. Practically, it showcases that a strict specification of the support conditions and load application configuration is necessary, for the experimental results to be consistent and comparable.

After specifying M^*, consider the critical bending moment M_o (figure 2a) at which circumferential-tension-induced splitting occurs. Cause of the circumferential tension is moment M^* (figure 2b). Note that the bending moment M^* induces bending of the culm wall in the plane of the cross-section, while M_o is the moment that causes the deflection of the longitudinal axis of the culm. Throughout this study, moments with "*" refer to bending of the culm wall in the plane of the cross-section. Following the procedure described in [20], the resulting expressions of M_o normalised with $A^{1.5}$, are:

$$\frac{M_{o,1}}{A^{1.5}} = 0.1364 \cdot \sqrt{E_\parallel \sigma_{\perp u}} \cdot \left(1 - 0.7012 \cdot \frac{\sigma_{\perp u}}{E_\perp} \cdot \phi \right) \tag{11}$$

$$\frac{M_{o,2}}{A^{1.5}} = 0.1114 \cdot \sqrt{E_\parallel \sigma_{\perp u}} \cdot \left(1 - 0.4680 \cdot \frac{\sigma_{\perp u}}{E_\perp} \cdot \phi \right) \tag{12}$$

6

$$\frac{M_{o,3}}{A^{1.5}} = 0.1041 \cdot \sqrt{E_\parallel \sigma_{\perp u}} \cdot \left(1 - 0.4086 \cdot \frac{\sigma_{\perp u}}{E_\perp} \cdot \phi\right) \tag{13}$$

$$\frac{M_{o,4}}{A^{1.5}} = 0.1547 \cdot \sqrt{E_\parallel \sigma_{\perp u}} \cdot \left(1 - 0.9024 \cdot \frac{\sigma_{\perp u}}{E_\perp} \cdot \phi\right) \tag{14}$$

where A is the cross-section area and subscripts 1-4 denote each of the load cases 1-4 (figure 3). Equations (11)-(14) associate bending moment M_o with shape factor ϕ and bamboo circumferential tensile strength $\sigma_{\perp u}$. For more details on their derivation, the reader can refer to Appendix A. Note that the derivation of equations (11)-(14) assumes a thin-walled section. However, thick-walled sections ($\phi < 5$) are not uncommon among bamboo species. In a thick-walled section case, the shift of the neutral axis position towards the centre of curvature of the curved beam is more prominent, compared to a thin-walled section [28]. That leads to lower tensile circumferential stresses at the points of positive M^* (inner side of the culm), and higher tensile circumferential stresses at the points of negative M^* (outer side of the culm) (figure 4), compared to the predictions of the present analysis (which ignores the neutral axis shift, refer also to Appendix A). Hence, equations (11)-(14), which assume failure at $\omega = 0^o$ (positive M^*, figure 4) are likely conservative.

3.2. Splitting induced by shear

Shear-induced splitting occurs at $\omega = 90^o$, since this is where maximum shear stress appears. In a circular tube, the value of maximum shear stress, accounting for the effect of cross-section shape is [29]:

$$\tau_{max} = \left(2 + \frac{1}{\phi}\right)\frac{V}{A} \tag{15}$$

where ϕ is the shape factor (equation (1)), V is the shear force and A is the cross-section area. In the four-point bending test (figure 2), under load P:

$$V = \frac{M_s}{L} \tag{16}$$

where L is the shear span length and M_s the bending moment at the time of shear failure. Assuming that L is n times the culm diameter $D = 2R$:

$$V = \frac{M_s}{2nR} \tag{17}$$

Substituting equation (17) into equation (15), substituting τ_{max} with shear strength parallel to the fibres $\tau_{u\parallel}$, and rearranging:

$$\frac{M_s}{A} = \frac{2nR\tau_{u\parallel}}{2 + \frac{1}{\phi}} \tag{18}$$

Subsequently, in order to have the same normalisation as in equations (3), (4) and (11)-(13), we divide both sides with $\sqrt{A} = \sqrt{2\pi Rt}$, which leads to the final version of the moment equation for shear-induced splitting:

$$\frac{M_s}{A^{1.5}} = \frac{n\tau_{u\parallel}\sqrt{2}}{\left(2 + \frac{1}{\phi}\right)\sqrt{\pi}}\sqrt{\phi} \tag{19}$$

Equation (19) associates the bending moment of shear failure (M_s) with shear strength parallel to the fibres $\tau_{u\parallel}$, shape factor ϕ and shear span length (taken into account with the dimensionless parameter n).

Table 1: Bamboo properties utilised for the construction of the failure maps (table values in MPa)

	Moso (specimen ML3)	Guadua	Kao Jue
$E_\parallel$	12320 [13]	17204 [14]	18500 [11]
$E_\perp$	1355 [30]	864 [30]	429 [31]
$\sigma_{u\parallel}$	72.2 [13]	58.0 [32]	69.0 [11]
$\sigma_{\perp u}$	3.0 [13]	3.7 [30]	17.0 [31]
$\tau_{u\parallel}$	21.8 [13]	12.0 [32]	19.4 [21]

3.3. Failure map

Figure 5 illustrates the failure maps constructed from equations (3), (4), (11)-(14) and (19) for Moso (*Phyllostachys pubescens*), Guadua (*Guadua angustifolia* Kunth) and Kao Jue (*Bambusa pervariabilis*) bamboo. All three species are used for similar technical applications, but their material and geometrical properties vary. Table 1 shows the material properties used to construct the failure maps. All material properties of Table 1 correspond to dried culms, of age and moisture content as in Table B.4 (Appendix B). For Moso bamboo, most of the adopted values ($E_\parallel$, $\sigma_{u\parallel}$, $\tau_{u\parallel}$) are specific to the reference culm (specimen ML3 [13]).

Figure 5 shows that Brazier moment M_B is not critical to failure for typical bamboo property values. This is in agreement with experimental studies [2, 12–14], where there is no evidence of cross-section ovalisation. Shear parallel to the fibres is also not critical (figure 5), even for short shear spans (n=5, hence, shear span length equal to 5 culm diameters). According to figure 5, considering typical material properties and culm shape factors, compression in the longitudinal direction is of concern for Guadua and Kao Jue, but not for Moso. For longitudinal compression to be critical for Moso, the cross-section would need to be significantly thick-walled ($\phi = 1.0 \sim 2.0$), which is not common for this species. Therefore, determining factor for the failure of a Moso bamboo culm with material properties similar to the culm under consideration (specimen ML3) is tension perpendicular to the fibers, regardless of the culm's shape factor. This is in agreement with numerical results for specimen ML3 [13]. On the contrary, Kao Jue is more likely to fail in longitudinal compression for typical shape factor values of this species ($\phi = 3.0 \sim 4.0$, [11, 21, 31]). Lastly, Guadua could either fail in longitudinal compression or in circumferential tension, depending on the shape factor (typical values ϕ=3.0∼6.0, [14, 33]). The critical shape factor ϕ_{cr}, at which the failure mode changes from longitudinal compression to circumferential tension, occurs equating equation (4) with each of the equations (11)-(14) and solving for ϕ:

$$\phi_{cr} = \left[\frac{E_\perp}{2b\sigma_{\perp u}} \left(\sqrt{ \frac{\sigma_{u\parallel}^2}{8\pi a^2 E_\parallel \sigma_{\perp u}} + 4b\frac{\sigma_{\perp u}}{E_\perp} } - \frac{\sigma_{u\parallel}}{a\sqrt{8\pi E_\parallel \sigma_{\perp u}}} \right) \right]^2 \tag{20}$$

where $a = 0.1364; 0.1114; 0.1041; 0.1547$ and $b = 0.7012; 0.4680; 0.4086; 0.9024$, are the coefficients of equations (11)-(14) for Cases 1∼4, respectively.

The results of this section regarding failure by (circumferential-tension-induced) longitudinal splitting are surprising, since one would expect species with higher mechanical anisotropy (ratio $E_\parallel/E_\perp$, Table 1), such as Kao Jue, to split more easily. This is because higher mechanical anisotropy leads to more prominent ovalisation, and thus more significant circumferential stresses [20]. However, Kao Jue has significantly higher circumferential tensile strength than Moso (Table 1), and thus is more resistant to splitting induced by circumferential tension; hence the observed failure by longitudinal compression instead.

In general, considering typical bamboo material and geometrical properties, Brazier instability or shear failure are unlikely (figure 5). However, whether culm wall buckling due to longitudinal compression occurs before circumferential-
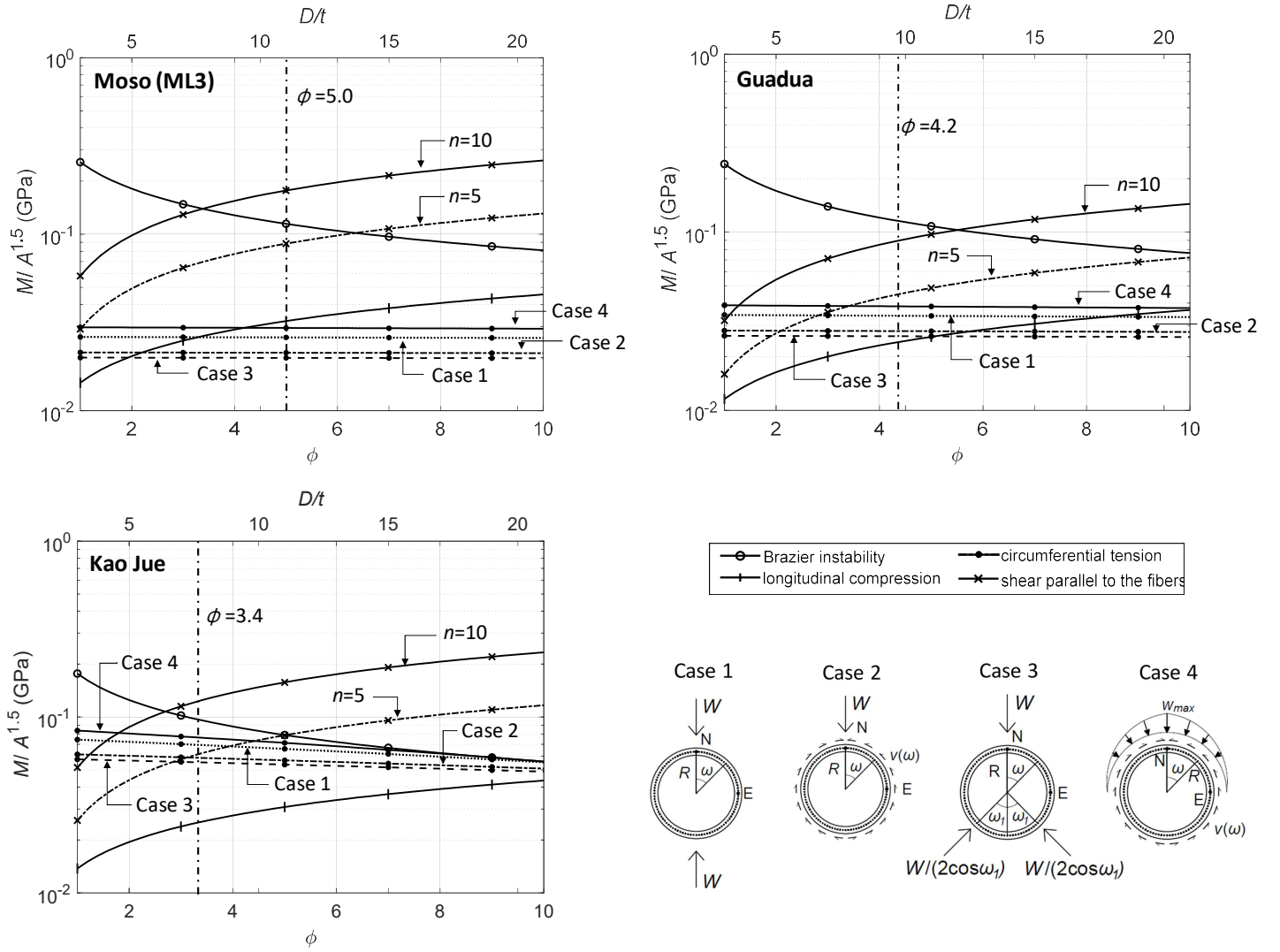
Figure 5: Failure maps of the critical bending moment of various bamboo species, versus shape factor ϕ and ratio of external diameter D to thickness t. Typical average values for ϕ are indicated on the graphs. For shear failure, curves for two shear span lengths are provided (n=5 and n=10, equation (19)).

tension-induced splitting, depends on the cross-section shape factor and the material properties (figure 5, equation (20)). This is in agreement with the experimental observations of [13] and partly in agreement with [14]. More specifically, the extensive experimental program of Trujillo et al [14] showed that splitting and longitudinal compression are the most common failure modes, and attributed splitting to shear (as opposed to circumferential tension), as it always occurred at the shear span [14]. A possible explanation is that there is interaction between circumferential tension and shear, which accelerates failure and produces a mixed-mode crack at the shear span.

An additional apparent inconsistency between the present analysis and the experimental observations is that the analysis herein assumes failure at position N ($\omega = 0^o$, point of maximum moment M^*), while in the experiments splitting usually occurs at position E ($\omega = 90^o$, figure 3). However, the failure map of figure 5 does not consider tension-shear interaction and, additionally, it examines failure initiation, not the crack propagation afterwards. This means that small unnoticeable cracks could initially appear at either position, but propagate faster at $\omega = 90^o$. This is because, while M^* is maximum at $\omega = 0^o$, there is no shear parallel to the fibres at that location. In contrast, at $\omega = 90^o$, the shear parallel to the fibres is maximum, while the value of M^* is significant (figure 3). The 'clicking' sounds observed in experiments [13], at the point where the stiffness of the experimental force-displacement curve is declining, supports the assumption of small unnoticeable cracks that appear much earlier than the eventual splitting failure. This however requires further
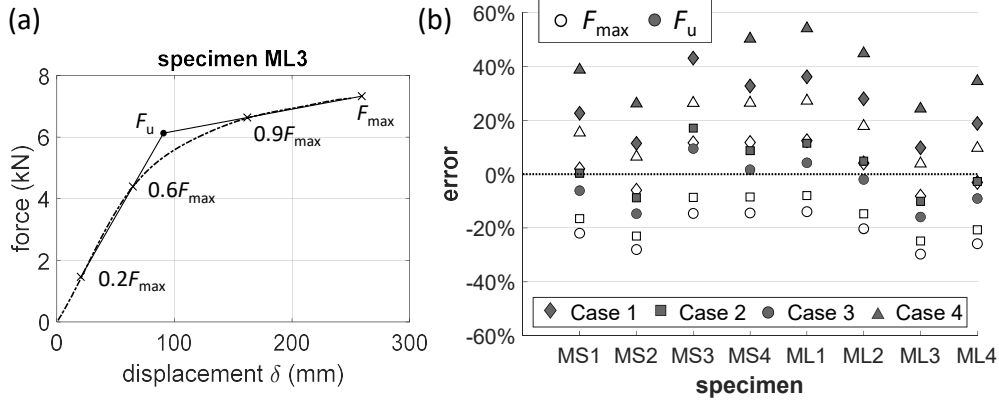
Figure 6: a) Failure load (F_u) determination, b) Accuracy of failure (F_u) and maximum (F_{max}) load prediction for Moso bamboo. Grey markers indicate the error compared to F_u, white markers indicate the error compared to F_{max}.

Table 2: Experimental failure loads and corresponding analytical predictions for Cases 1∼4

specimen no[a]	$E_\parallel{}^a$ (MPa)	ϕ^a	$F_{max}{}^a$ (kN)	$F_u{}^a$ (kN)	$F_{u,an}{}^b$ Case 1 (kN)	$F_{u,an}{}^c$ Case 2 (kN)	$F_{u,an}{}^d$ Case 3 (kN)	$F_{u,an}{}^e$ Case 4 (kN)
MS1	15420	4.62	5.68	4.72	5.79	4.72	4.43	6.55
MS2	13580	4.50	6.37	5.38	5.99	4.91	4.59	6.78
MS3	12657	3.79	5.17	4.03	5.77	4.72	4.41	6.53
MS4	12247	5.09	5.15	4.34	5.76	4.72	4.41	6.51
ML1	11243	4.45	5.97	4.93	6.71	5.49	5.14	7.60
ML2	10068	5.21	4.01	3.26	4.17	3.42	3.20	4.72
ML3	12501	5.00	7.33	6.13	6.73	5.51	5.15	7.61
ML4	12667	4.44	5.86	4.78	5.68	4.65	4.35	6.43

[a]ref. [13], [b]equation 11, [c]equation 12, [d]equation 13, [e]equation 14

verification, as these could also be pre-existing cracks (e.g., because of the drying process or ambient humidity variations), that start propagating. These cracks (or, if the culm is intact, residual stresses, that cause cracks at small additional loads), are likely to form during moisture content variations. This is because of the difference in the drying speeds between the inner and the outer side of the bamboo culm wall (that is attributed to the difference in density of the two sides), which causes shrinkage of the two sides at different rates [34]. A slower drying procedure, or even harvesting the culms during a season where the saps within are at their lowest (and thus the culms' moisture content is reduced), could potentially improve the mechanical performance of the dried material [34]. However, more research is needed to determine the extent of the improvement and the practicality of the solution in the context of bamboo for structural applications.

4. Analytical prediction of the failure load

After establishing the most probable failure cause of bamboo culms subjected to bending, this Section examines whether it is possible to use this information to predict analytically the failure load. The goal is to determine the accuracy of the analytical predictions and, in the case of longitudinal splitting, to evaluate which is the most suitable load assumption (Cases 1∼4) to predict the failure load. To this end, this study considers three bamboo species; Moso, Kao Jue and Guadua, and pertinent experimental results from literature.

For Moso bamboo, Table 2 compares the analytical failure load predictions $F_{u,an}$ with the experimental results of [13]. As these results refer to four-point bending test, the failure load $F_{u,an}$ occurs as $2M/L$, after obtaining the failure moment M from equations (11)-(14), where L is the shear span length (figure 2a). Recall that each of the equations (11)-(14) assumes a different load case (figure 3), that creates circumferential stresses, which lead to splitting. There

10

Table 3: Failure moment prediction for Kao Jue

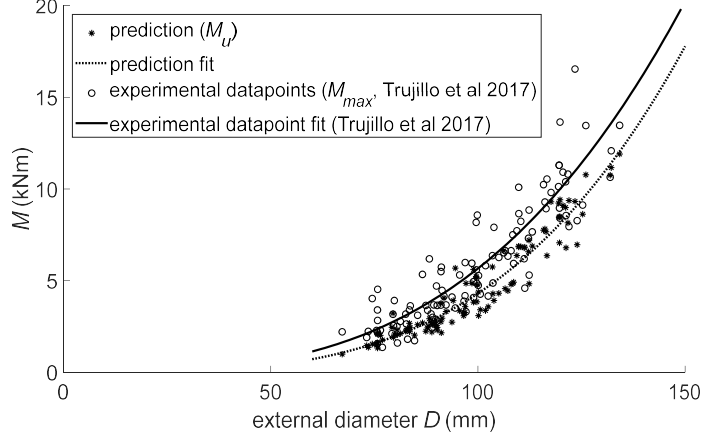| study	$E_\parallel$ (MPa)	MOR (MPa)	external diameter D (mm)	thickness (mm)	experimental moment M_u (kNm)	predicted moment M_f (kNm)	error $\frac{M_f - M_u}{M_u}$
[11]	18500	82.0	40.7	5.2	0.368	0.355	-3.5%
[21]	12104	52.2	47.7	5.9	0.371	0.361	-2.6%

Figure 7: Comparison between experimental results [14] and predicted values for Guadua.

are two experimental values of interest for each specimen; the maximum load F_{max} and a nominal failure load F_u. The latter occurs after constructing an equivalent bilinear curve from the experimental curve (figure 6a). The first line of the bilinear curve connects the datapoints that correspond to 20% and 60% of the maximum load F_{max} (which are the points that define the assumed linear-elastic region [15]), while the second line connects the datapoints that correspond to 90% and 100% of F_{max}. F_u is the force at the intersection of the two lines. Figure 6b illustrates the error between the analytical prediction and the experimental values (defined as $(F_{u,an} - F_{exp})/F_{exp}$, where F_{exp} is F_{max} or F_u) for each load case and each specimen. It shows that equation (11) (Case 1) is more suitable for predicting maximum load F_{max}, while equations (12) and (13) (Cases 2 and 3) are more suitable for predicting nominal failure load F_u, with equal accuracy. Equation 14 predicts too high failure loads, overestimating F_{max} by 16.7% and F_u by 41.9%. Average absolute error for the prediction of F_{max} using equation (11) is 7.4%, whereas for the prediction of F_u the average absolute error is 8.0% for equation (12) and 7.8% for equation (13).

For Kao Jue, (Table 3) compares the predicted failure moment M_f with pertinent experimental values of [11] and [21]. Both studies report the modulus of rupture (MOR) instead of the failure bending moment, hence herein we estimate the experimental failure bending moment M_u as:

$$M_u = MOR \cdot \frac{I}{R_o} \tag{21}$$

where I is the cross-section moment of inertia and R_o the external culm radius. For the calculation of I and R_o, we adopt the average geometrical properties reported in the pertinent studies (Table 3). The predicted failure moment M_f occurs as:

$$M_f = min\left(M_B, M_l, M_{o1}, M_s\right) \tag{22}$$

where M_B, M_l, M_{o1} and M_s as in equations (3), (4), (11 and (19). This analysis adopts the material property values of Table 1. Table 3 summarises the parameters and the results of the analysis. The prediction errors for [11] and [21] are -3.5% and -2.6% respectively. Thus, in the case of Kao Jue, utilising average geometrical and material properties leads to a slight underestimation of the average failure bending moment.

11

For Guadua bamboo, Figure 7 evaluates the proposed analytical prediction of the failure moment with pertinent experimental results [14]. The predicted values occur utilising actual geometrical data of the specimens tested in [14] and average material properties (Table 1). The predicted correlation between failure moment and external diameter shows the same trend as the corresponding experimental correlation. However, the analytical prediction tends to underestimate the experimental values (by 18% on average). A possible explanation is that the predicted failure moment refers to the bending moment of failure initiation ($M \approx M_u$), whereas the experimental moment refers to the maximum bending moment (M_{max}), which occurs after failure initiation.

Overall, given the uncertainties involved, the accuracy of the proposed equations is acceptable.

5. Stiffness loss

5.1. Effect of cracks

The appearance of small cracks when the stiffness of the experimental force-displacement curve progressively drops, likely means that these cracks play an important role on the stiffness loss. The extent of the stiffness loss depends on the number and position of the appearing cracks. In the case of a single crack, the culm cross-section transitions from a closed section to an open section, the shear centre shifts, and thus load P creates a torque about the shear centre. The work of this torque causes additional deflections, and thus can potentially contribute to a stiffness loss. However, the additional deflections are not significant, unless the crack extends to a substantial portion of the span length. This is because the torsional constant of the closed section is $J_{s,c} = 2\pi R^3 t$, which makes it $3\phi^2$ times higher than the torsional constant of the open section ($J_{s,o} = \frac{2}{3}\pi R t^3$). Thus, the torsional stiffness of a closed section is one to two orders of magnitude higher than that of an open section. Because of this relatively small magnitude, and of the complexity of the torsion problem, we will examine the stiffness loss due to a single crack at the side of a bamboo culm in a separate study. This section focuses on how two simultaneous cracks at the sides of the bamboo culm (figure 8b) affect its bending stiffness.

For the four-point bending test of figure 1, the deflection δ_b at the midspan because of the bending moment is:

$$\delta_b = \frac{23PL^3}{24E_\parallel I} \tag{23}$$

where L is the shear span length, equal to 1/3 of the total span length (figure 2a) and $I = \pi R^3 t$ for an intact section. Note that P in equation (23) corresponds to half of the total load (figures 1, 2a).

In the case of two simultaneous cracks at the sides of the culm, the bending stiffness changes. This is because, instead of a circular tube, the cross-section now consists of two C-shaped sections (figure 8b). The moment of inertia of a C-shaped thin-walled semi-circular section about a horizontal axis x_1 that passes through its centroid C (figure 8b) is:

$$I_C = R^3 t \left(\frac{\pi}{2} - \frac{32}{9\pi} \right) \tag{24}$$

The moment of inertia I_{CC} of a cross-section consisting of two of these sections as in figure 8b is:

$$I_{CC} = 2I_C = R^3 t \left(\pi - \frac{64}{9\pi} \right) \tag{25}$$
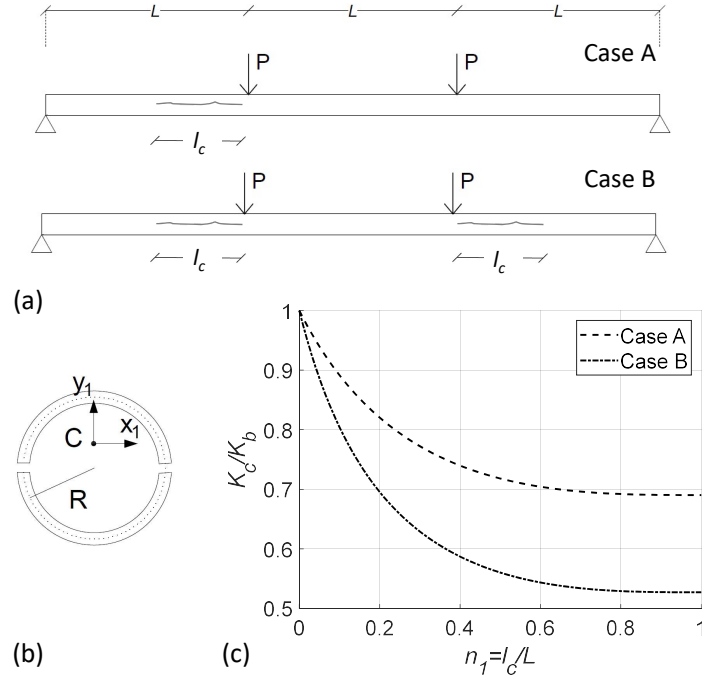
Figure 8: Effect of crack length on bending stiffness. a) Crack locations considered, b) Assumed culm cross-section (cracks at both sides), c) Effect of crack length on the bending stiffness

I_{CC} compares with the initial moment of inertia of a closed circular tube $I = \pi R^3 t$ as:

$$\frac{I_{CC}}{I} = 1 - \frac{64}{9\pi^2} \Rightarrow I_{CC} = 0.28I \tag{26}$$

This means that the bending stiffness drops by 72% if cracks open on both sides of the culm. Note however that this calculation (equation (25)) assumes that the two parts of the section are independent, and therefore they do not form a composite section. Confining steel rings can restore composite action, thus minimising the effect the cracks on the bending stiffness [13]. Hence, the present analysis does not account for the mitigating (for stiffness loss) effect of friction on the crack interface, and thus it is a lower-bound approach.

To get a better understanding on how the crack length affects the stiffness, consider a culm subjected to four-point flexure, and cracks initiating at the cross-sections under the load application points and propagating towards the closest support (figure 8a). Basis for this assumption is that, according to experimental observations (e.g., [14]), the shear span is the most common position of crack occurrence. At each cracked position along the beam, assume two cracks, one at each side, so that the cracked cross-section is that of figure 8b. Consider two cases, one with the cracks appearing at one shear span (initiating under one load application point, case A), and one where the cracks appear at both shear spans simultaneously (case B) (figure 8a). Utilising the virtual work method, the deflection at the midspan is:

$$\delta_{cA} = \int_0^{L-l_c} \frac{Pz^2}{2E_\parallel I} dz + \int_{L-l_c}^{L} \frac{Pz^2}{2E_\parallel I_{CC}} dz + \int_{L}^{1.5L} \frac{PLz}{2E_\parallel I} dz + \frac{23PL^3}{48E_\parallel I} \tag{27}$$

for case A and

$$\delta_{cB} = 2 \int_0^{L-l_c} \frac{Pz^2}{2E_\parallel I} dz + 2 \int_{L-l_c}^{L} \frac{Pz^2}{2E_\parallel I_{CC}} dz + 2 \int_{L}^{1.5L} \frac{PLz}{2E_\parallel I} dz \tag{28}$$

for case B. Calculating the integrals, taking into account equation (26), and setting $l_c = n_1 L$ (with l_c being the crack

13

length and L the shear span length):

$$\delta_c = \frac{23PL^3}{24E_\parallel I}\left[1 + b_i n_1\left(n_1^2 - 3n_1 + 3\right)\right] \tag{29}$$

where b_i is a constant, equal to 0.45 for case A and 0.90 for case B. Subsequently, taking into account equation (23), we associate the ratio of the cracked (K_c) over the initial (K_b) bending stiffness with the crack length:

$$\frac{K_{c,i}}{K_b} = \left[1 + b_i n_1\left(n_1^2 - 3n_1 + 3\right)\right]^{-1} \tag{30}$$

Figure 8c visualises equation (30). It shows that the stiffness drops rapidly with crack propagation, and reaches approximately 95% of its final value when the crack length is equal to half the shear span length ($n_1 \approx 0.5$). That final value is 69% of the initial bending stiffness for case A and 53% for case B, indicating that the stiffness loss is significant even for relatively short crack lengths.

5.2. Geometric non-linearities

Another parameter that may affect the stiffness is geometric non-linearities. Bamboo is a flexible material, therefore it exhibits large deformations when in flexure. To determine whether the deformations during the four-point bending test are large enough to affect the stiffness, consider the parabolic beam of figure 9a, instead of a straight beam. Basis for this assumption is that the parabola is a good approximation for the deformed shape of a beam under four-point flexure. Because of symmetry, we consider only half of the beam. If (z, y) are the coordinates of each point on the beam axis, and considering as origin of the coordinate system the shear hinge (figure 9a), the y-coordinate (vertical axis) as a function of the z-coordinate (horizontal axis) is $y = az^2$, where a is:

$$a = \frac{h}{l^2} \tag{31}$$

In equation (31), h is the vertical distance between the supports of the parabolic (half) beam (or, the total deflection of the initially horizontal beam), and l is the horizontal distance between the supports, after applying symmetry (figure 9a). Herein, l corresponds to a length 1.5 times the shear span length ($l = 3L/2$). Therefore, load P is applied at $z = l/3$. The analysis that follows assumes that load P and the roller support at point B (figure 9a) are perpendicular to the beam. This is representative of the experimental conditions.

To determine the deflection δ_p of the parabolic beam, this section uses the Castigliano theorem. Applying a vertical force F on the middle of the culm (which is the point of the deflection of interest), leads to a force $F/2$ on the shear hinge support of the parabolic (half) beam under consideration (figure 9a). According to the Castigliano theorem, the deflection δ_p of the parabolic beam is:

$$\delta_p = 2\int \frac{M\left(s\right)}{E_\parallel I} \cdot \frac{dM}{dF} ds + 2\int \frac{N\left(s\right)}{E_\parallel A} \cdot \frac{dN}{dF} ds \tag{32}$$

where M is the bending moment, N is the axial force and s is the coordinate along the length of the beam:

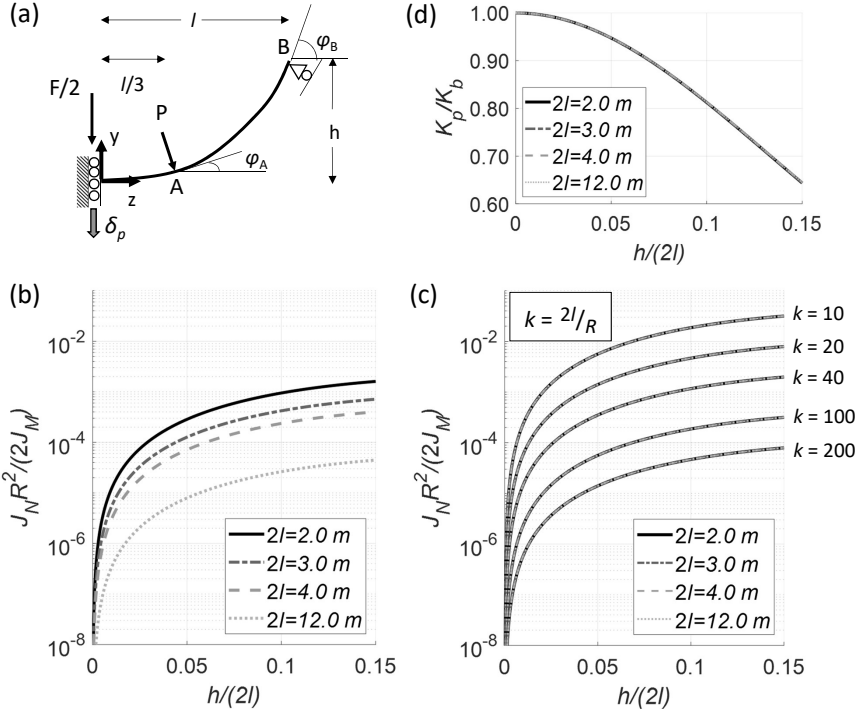$$s = \int \sqrt{1 + \left(\frac{dy}{dz}\right)^2} dz = \int \sqrt{1 + 4a^2z^2} dz \tag{33}$$

14

Figure 9: Effect of large deformations on the bending stiffness for various span lengths. Terms $J_N R^2/2$ and J_M demonstrate respectively the contributions of axial force and bending moment on the total deflection of the parabolic beam. a) Parabolic beam under consideration, b) Effect of span length on ratio $J_N R^2/(2J_M)$ ($R=45$ mm), c) Effect of ratio $k = 2l/R$ on $J_N R^2/(2J_M)$, d) Stiffness loss versus normalised deflection: K_b is the initial bending stiffness of the straight beam, K_p is the bending stiffness of the (deformed) parabolic beam.

Therefore:

$$\frac{ds}{dz} = \sqrt{1 + 4a^2 z^2} \tag{34}$$

and equation (32) becomes:

$$\delta_p = 2 \int \frac{M(z)}{E_\parallel I} \cdot \frac{dM}{dF} \cdot \sqrt{1 + 4a^2 z^2} dz + 2 \int \frac{N(z)}{E_\parallel A} \cdot \frac{dN}{dF} \cdot \sqrt{1 + 4a^2 z^2} dz \tag{35}$$

where:

$$M(z) = \begin{cases} \frac{F}{2} \cdot [l - z + \tan\varphi_B \cdot (h - y)] + P_y \cdot \left[\frac{2l}{3} + \tan\varphi_B \cdot (h - y)\right] + P_z \cdot (y - y_A), & 0 \leq z < \frac{l}{3} \\ \left(P_y + \frac{F}{2}\right) \cdot [l - z + \tan\varphi_B \cdot (h - y)], & \frac{l}{3} < z \leq l \end{cases} \tag{36}$$

$$N(z) = \begin{cases} (P_z - P_y \tan\varphi_B) \cdot \cos\varphi - \frac{F}{2} \cdot (\sin\varphi + \tan\varphi_B \cdot \cos\varphi), & 0 \leq z < \frac{l}{3} \\ -\left(P_y + \frac{F}{2}\right) \cdot (\sin\varphi + \tan\varphi_B \cdot \cos\varphi), & \frac{l}{3} < z \leq l \end{cases} \tag{37}$$

In equations (36) and (37), P_y is the vertical component of load P, P_z is the horizontal component of load P, and φ is the angle between the beam axis and the horizontal axis at each point along the beam. Thus, φ_A and φ_B are the angles between the beam axis and the horizontal axis at points A (load application point) and B (roller support) respectively (figure 9a). From equations (36) and (37):

$$\frac{dM}{dF} = \frac{1}{2} [l - z + \tan\varphi_B \cdot (h - y)], \quad 0 \leq z \leq l \tag{38}$$

$$\frac{dN}{dF} = -\frac{1}{2} (\sin\varphi + \tan\varphi_B \cdot \cos\varphi), \quad 0 \leq z \leq l \tag{39}$$

15

Substituting equations (36)-(39) into equation (35) and setting $F = 0$:

$$\delta_p = \frac{2P}{E_\parallel I} J_M + \frac{2P}{E_\parallel A} J_N \tag{40}$$

where:

$$2J_M = \int_0^{l/3} \left\{ 2\cos\varphi_A \left[\frac{l}{3} + a^2 l \left(l^2 - z^2 \right) \right] + a\sin\varphi_A \left(z^2 - \frac{l^2}{9} \right) \right\} \left[l - z + 2a^2 l \left(l^2 - z^2 \right) \right] \sqrt{1 + 4a^2 z^2} dz +$$
$$+ \int_{l/3}^l \cos\varphi_A \cdot \left[l - z + 2al \left(l^2 - z^2 \right) \right]^2 \cdot \sqrt{1 + 4a^2 z^2} dz \tag{41}$$

$$2J_N = -\int_0^{l/3} \left(\sin\varphi_A - 2al\cos\varphi_A \right) \left(\sin\varphi + 2al\cos\varphi \right) \cos\varphi \sqrt{1 + 4a^2 z^2} dz +$$
$$+ \int_{l/3}^l \cos\varphi_A (\sin\varphi + 2al \cdot \cos\varphi)^2 \sqrt{1 + 4a^2 z^2} dz \tag{42}$$

and

$$\varphi(z) = \arctan\frac{dy}{dz} = \arctan(2az) \tag{43}$$

Integrals J_M and J_N correspond respectively to the contribution of the bending moment and axial force to the total deflection. Further considering that, for a thin-walled circular tube, $E_\parallel I / E_\parallel A = R^2/2$, and rearranging, equation (40) becomes:

$$\frac{E_\parallel I \delta_p}{2P} = \frac{E_\parallel I}{K_p} = J_M + \frac{R^2}{2} J_N \tag{44}$$

where K_p is the stiffness of the parabolic beam for a given shape parameter a. Combining equations (44) and (23):

$$\frac{K_p}{K_b} = \frac{\frac{23}{162} l^3}{J_M + \frac{R^2}{2} J_N} \tag{45}$$

where l is half the total span length (figure 9a). Inspecting equation (45), it appears that, for thin-walled tubes subjected to four-point flexure, the loss of stiffness because of non-linear geometric effects depends on the tube radius and the span length.

However, the importance of the tube radius depends on the relative significance of terms $J_N R^2/2$ (contribution of axial force) and J_M (contribution of bending moment). If $J_N R^2/2$ is sufficiently small compared to J_M, radius R practically does not affect the stiffness loss induced by non-linear geometric effects. Indeed, figure 9b illustrates that, for the radius of the reference culm (R=45 mm), term $J_N R^2/2$ is at least three orders of magnitude smaller than J_M, even for significant deflections h. Figure 9b also shows that, for a fixed radius value, the axial force term $J_N R^2/2$ becomes more significant (compared to the bending moment term J_M) at shorter span lengths. To investigate this further, figure 9c illustrates how ratio $2l/R$ (total span length over tube radius) affects the relative significance of terms $J_N R^2/2$ and J_M, given by the ratio thereof. It shows that ratio $J_N R^2/(2J_M)$ is the same, regardless of span length, as long as $2l/R$ remains constant. It also shows that, at large deflections, $J_N R^2/2$ is negligible compared to J_M when the total-span-length-to-radius ratio is sufficiently large ($2l/R \geq 20$). As expected, at small deflections, $J_N R^2/2$ is always negligible, regardless of the value of $2l/R$. Therefore, radius R does not affect the stiffness loss induced by non-linear geometric effects, unless $2l/R < 20$ (short beams).

Regarding the effect of total span length ($2l$), figure 9d plots equation (45) for various span lengths. It correlates the stiffness of the parabolic beam (K_p), normalised with the initial bending stiffness of a straight beam (K_b), with parameter
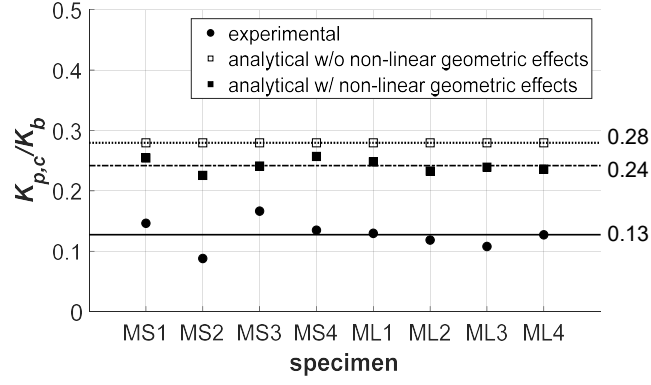
Figure 10: Comparison between experimental and predicted stiffness loss, assuming two cracks at the sides of the culm.

h (which corresponds to the total deflection of the straight beam). Figure 9d shows that, considering the total deflection as a percentage of the total span length (normalising parameter h with the total span length $2l$), the percentage of stiffness lost at each deflection stage (compared to the initial stiffness) is the same, regardless of span length. This means that, regardless of span length, there is a single equation that describes the stiffness loss associated with non-linear geometric effects as a function of the normalised deflection. However, the feasibility of obtaining a closed-form analytical solution for K_p/K_b as a function of $h/(2l)$, that is simultaneously elegant, is doubtful, because of the complexity of integral J_M (equation (41)). An alternative is to fit a curve on the data points of figure 9d. The following third-degree polynomial is a perfect fit (coefficient of determination $r^2=1.0$):

$$\frac{K_p}{K_b} = 62.18\left(\frac{h}{2l}\right)^3 - 25.81\left(\frac{h}{2l}\right)^2 + 0.10\frac{h}{2l} + 1.00 \tag{46}$$

Equation (46) holds true for any span length, provided that $2l/R \geq 20$ (so that axial force term $R^2 J_N/2$ is negligible compared to bending moment term J_M, equation (45)). For the reference bamboo culm, and at a deflection of 8.3% of the initial span length ($\delta=250$ mm, figure 1c), it occurs form figure 9d and equation (46) that the stiffness is 13.5% lower compared to the initial stiffness ($K_p/K_b=86.5\%$), because of geometric non-linearities.

5.3. Evaluation of predicted stiffness loss

This section compares the stiffness loss predicted analytically with pertinent experimental results. Initially, it estimates the experimental stiffness loss based on the force-displacement curves of [13], as the ratio of final over initial stiffness. The initial and final stiffness values occur from the corresponding slopes of the bilinear curve branches described in Section 4. This section compares the experimental stiffness loss of each specimen with two analytically predicted values; with and without taking into account non-linear geometric effects. For the case of cracks and non-linear geometric effects combined, let K_b be the bending stiffness of the intact culm, $K_{b,c}$ the bending stiffness of a cracked culm and $K_{p,c}$ the stiffness of a cracked culm taking into account non-linear geometric effects. The ratio that defines the stiffness loss of interest is $K_{p,c}/K_b$. It follows that:

$$\frac{K_{p,c}}{K_b} = \frac{K_{p,c}}{K_{b,c}} \cdot \frac{K_{b,c}}{K_b} \tag{47}$$

where $K_{p,c}/K_{b,c}$ occurs for each specimen from equation (46), taking h=maximum experimental deflection and l=1500 mm. Additionally, assuming that the cracks extend on the entire span length (which is in line with experimental observations [13]), $K_{b,c}/K_b = 0.28$ (equation (26)).

Figure 10 illustrates the results of the stiffness loss analysis. The predicted final stiffness is on average 11%K_b higher

17

than the experimental final stiffness. Both the analytical expression and the experimental results indicate a drastic stiffness loss near the ultimate load, however the analytical expression underestimates the stiffness loss. A possible reason for this discrepancy lies in the simplifications made for the analytical equations; the equations assume linear-elastic material and refer to a specific case of crack number and position (two cracks, one at each side of the culm).

6. Discussion and conclusions

The analysis presented herein showcases the complexity of bamboo culm flexure, which is a result of culm geometry, material properties, cracking, and non-linear geometric effects. The study focuses on estimating analytically two aspects of full-culm bamboo flexural member behaviour, that are of interest to pertinent design codes and testing standards; failure load and stiffness loss. The analytical derivations consider the bamboo culm as an orthotropic, thin-walled tube of constant diameter and thickness. The proposed modelling does not account for thick-walled cylinder cases or property gradation along the culm thickness, which could be topics of future research. Nevertheless, despite these limitations, the proposed approach approximates well the experimental behaviour of bamboo culms.

Specifically, the study initially determines analytically the failure loads for various failure modes (Brazier effect, longitudinal tension/compression failure and longitudinal splitting induced by shear or circumferential tension) as a function of the cross-section shape factor $\phi = R/t$ (culm geometry). Subsequently, the study identifies the critical failure mechanism for three bamboo species (Moso, Guadua and Kao Jue). It concludes that longitudinal splitting, caused mainly by circumferential tension, is the primary failure mechanism for Moso, while Kao Jue is more likely to fail in longitudinal compression. Guadua can fail in either of the two mechanisms, depending on the culm shape factor and material properties. In the case of longitudinal splitting, the presence of shear parallel to the fibres at areas with high circumferential tension likely accelerates failure, because of shear-circumferential tension interaction. Evaluating the accuracy of the predicted failure load values, the results indicate that the analytical expressions tend to underestimate the failure load. This is acceptable given the uncertainties in material properties, the problem assumptions, and the fact that shear-circumferential tension interaction is not taken into account. Regarding stiffness loss, the present work demonstrates that the primary cause is longitudinal splitting, with secondary cause being non-linear geometric effects at the large deflection stage. Therefore, quantifying stiffness loss largely depends on the position, length, and number of appearing cracks. These are not easy to specify experimentally, especially since stiffness starts declining at a stage where cracks are not yet apparent, earlier than eventual failure.

As a demonstration, the study considers the case of two simultaneous cracks at the sides of the culm. In that case, stiffness loss is substantial, even for short crack lengths. Cause of the stiffness loss is the significant reduction of flexural rigidity $(E_\parallel I)$, and in particular the cross-section moment of inertia I. Specifically, even when the cracks extend only from one load application point to the middle of the shear span, the stiffness drops by approximately 30%. At the extreme case where the cracks extend throughout the entire span, the stiffness loss is 72%. Additionally considering non-linear geometric effects, at the large deflection stage (that is, deflection at the middle of the culm equal to 8%-10% of the total span length), the total stiffness loss of a cracked culm compared to an intact culm is 76%. This value assumes a parabolic deformed shape which, while not strictly accurate, is a close approximation of the actual deformed shape of a beam under four-point flexure. In comparison, the average stiffness loss observed experimentally is 87%. The discrepancy between predicted and experimental stiffness is reasonable, given the uncertainties on actual crack number and position. Moreover, this study shows that the stiffness loss induced by non-linear geometric effects can be described as a function

of normalised (with the total span length) deflection by a single equation, regardless of the distinct values of span length and culm radius. This holds true as long as the ratio of total span length over culm radius is larger than 20.

The findings of this study point towards a need for confinement in full-culm bamboo flexural members. Confinement can potentially alleviate circumferential tensile stresses, thus postponing cracking that leads to stiffness loss. Additionally, even when cracks appear, it can enforce partial continuity of shear stresses at the interface, thus mitigating the negative effect cracks have on the flexural performance. Moreover, the fact that splitting plays a predominant role on the flexural member performance, showcases the importance of investigating bamboo fracture properties, in terms of failure initiation and crack propagation, especially under mixed-mode conditions (interaction between tension and shear). Lastly, the analysis highlights the significance of the manner in which the load is applied on the culms for culm failure, and thus it emphasises the need for particular specifications in bamboo testing standards (regarding support conditions and load application configuration), so that the experimental results are consistent and comparable.

Overall, this study provides analytical tools for the estimation of failure load and the quantification of stiffness loss for full culm bamboo flexural members. Importantly, the methodology presented herein is in line with the current tendency for a capacity-based approach in bamboo structure design. This is a crucial step towards the rational engineering design of bamboo flexural members.

Author contributions

T. Mouka: Conceptualisation, Methodology, Validation, Formal Analysis, Data Curation, Writing-Original draft, Writing-Review & editing, Visualisation. **E. G. Dimitrakopoulos:** Conceptualisation, Methodology, Resources, Writing-Review & editing, Supervision, Funding acquisition. **R. Lorenzo:** Conceptualisation, Writing-Review & editing, Supervision.

Data accessibility

This work does not include original experimental data.

Appendix A. Calculation of M_o as a function of circumferential tensile strength $\sigma_{\perp u}$

Herein we follow the same procedure as in [20]. The procedure initially identifies the critical bending moment M^* for each load case (figure 3). In this study, it is the maximum value of M^* for all cases, occurring at $\omega = 0^o$ (point N, under load W, figs. 3 and 4). It subsequently associates M^* with the material's circumferential tensile strength $\sigma_{\perp u}$ and then with the change in the vertical diameter D_V (figure A.11a). Thus, D_V, which is a measure of the cross-section ovalisation,
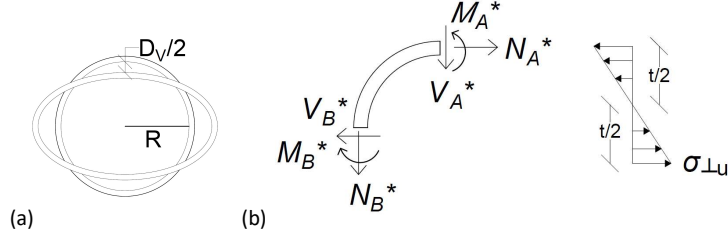
Figure A.11: a) Schematic representation of change in the vertical diameter D_V, b) Forces and normal stress in the circumferential direction

occurs as a function of $\sigma_{\perp u}$. Finally, it associates D_V with longitudinal curvature and ultimately with bending moment M_o. Hence, eventually M_o occurs as a function of the circumferential tensile strength $\sigma_{\perp u}$.

Starting with M^*, its maximum value for Cases 1-4 respectively is [28]:

$$M_{N,1}^* = \frac{WR}{\pi} \tag{A.1}$$

$$M_{N,2}^* = \frac{3WR}{4\pi} \tag{A.2}$$

$$M_{N,3}^* = \frac{WR}{\pi} \cdot \left(\frac{\sqrt{2}+1}{2} - \frac{\pi}{8} \right) \tag{A.3}$$

$$M_{N,4}^* = \frac{WR}{\pi} \cdot \left(\frac{5}{4} + \frac{\pi}{4} - \frac{3\pi^2}{16} \right) \tag{A.4}$$

At failure, M_N^* as a function of circumferential tensile strength $\sigma_{\perp u}$ (ignoring the shift in the neutral axis due to the curvature of the beam) is (figure A.11b):

$$M_N^* = \frac{1}{6}\sigma_{\perp u}t^2 \tag{A.5}$$

Combining each of the equations (A.1)-(A.4) with equation (A.5), we get WR with respect to $\sigma_{\perp u}$ for each case:

$$(WR)_1 = \frac{\pi}{6}\sigma_{\perp u}t^2 \tag{A.6}$$

$$(WR)_2 = \frac{2\pi}{9}\sigma_{\perp u}t^2 \tag{A.7}$$

$$(WR)_3 = \frac{4\pi}{3\left[4\left(\sqrt{2}+1\right)-\pi\right]} \cdot \sigma_{\perp u}t^2 \tag{A.8}$$

$$(WR)_4 = \frac{8\pi}{3\left(2+\pi\right)\left(10-3\pi\right)} \cdot \sigma_{\perp u}t^2 \tag{A.9}$$

For a given load W, the change in the vertical diameter D_V (figure A.11a), normalised with $2R$, is for each case [28]:

$$\zeta_1 = \frac{D_{V1}}{2R} = \frac{WR^2}{E_\perp I} \cdot \left(\frac{1}{\pi} - \frac{\pi}{8} \right) \tag{A.10}$$

$$\zeta_2 = \frac{D_{V2}}{2R} = \frac{WR^2}{2E_\perp I} \cdot \left(\frac{1}{\pi} - \frac{\pi}{8} \right) \tag{A.11}$$

$$\zeta_3 = \frac{D_{V3}}{2R} = \frac{WR^2}{2E_\perp I} \cdot \left(\frac{\sqrt{2}+1}{\pi} - \frac{3\pi+4}{16} \right) \tag{A.12}$$

$$\zeta_4 = \frac{D_{V4}}{2R} = -\frac{WR^2}{E_\perp I} \cdot \frac{\pi-3}{8} \tag{A.13}$$

20

The dimensionless change in vertical diameter ζ is negative in all cases, which indicates a diameter reduction. Substituting equations (A.6)-(A.9) into equations (A.10)-(A.13) respectively, ζ occurs with respect to $\sigma_{\perp u}$:

$$\zeta_1 = -0.4675 \cdot \frac{\sigma_{\perp u}}{E_\perp} \cdot \frac{R}{t} \tag{A.14}$$

$$\zeta_2 = -0.3120 \cdot \frac{\sigma_{\perp u}}{E_\perp} \cdot \frac{R}{t} \tag{A.15}$$

$$\zeta_3 = -0.2724 \cdot \frac{\sigma_{\perp u}}{E_\perp} \cdot \frac{R}{t} \tag{A.16}$$

$$\zeta_4 = -0.6016 \cdot \frac{\sigma_{\perp u}}{E_\perp} \cdot \frac{R}{t} \tag{A.17}$$

ζ can be linked with longitudinal curvature C as [20]:

$$|\zeta| = \frac{4}{3}c^2 \tag{A.18}$$

where c is a dimensionless curvature:

$$c^2 = \frac{3}{4}\frac{R^4}{t^2}\frac{E_\parallel}{E_\perp}C^2 \tag{A.19}$$

Combining each of the equations (A.14)-(A.17) with equation (A.18):

$$c_1 = \left(0.3506 \cdot \frac{\sigma_{\perp u}}{E_\perp} \cdot \frac{R}{t}\right)^{1/2} \tag{A.20}$$

$$c_2 = \left(0.2340 \cdot \frac{\sigma_{\perp u}}{E_\perp} \cdot \frac{R}{t}\right)^{1/2} \tag{A.21}$$

$$c_3 = \left(0.2043 \cdot \frac{\sigma_{\perp u}}{E_\perp} \cdot \frac{R}{t}\right)^{1/2} \tag{A.22}$$

$$c_4 = \left(0.4512 \cdot \frac{\sigma_{\perp u}}{E_\perp} \cdot \frac{R}{t}\right)^{1/2} \tag{A.23}$$

Finally, we associate the dimensionless curvature c with bending moment M_o (figure 2a), which is the cause of the curvature [20]:

$$M_o = \frac{2\pi}{\sqrt{3}}Rt^2\sqrt{E_\parallel E_\perp} \cdot \left(c - 2c^3\right) \tag{A.24}$$

Substituting each of the equations (A.20)- (A.23) into equation (A.24):

$$M_{o,1} = 2.1480 \cdot (Rt)^{3/2} \cdot \left(E_\parallel \sigma_{\perp u}\right)^{1/2} \cdot \left(1 - 0.7012 \cdot \frac{\sigma_{\perp u}}{E_\perp} \cdot \frac{R}{t}\right) \tag{A.25}$$

$$M_{o,2} = 1.7548 \cdot (Rt)^{3/2} \cdot \left(E_\parallel \sigma_{\perp u}\right)^{1/2} \cdot \left(1 - 0.4680 \cdot \frac{\sigma_{\perp u}}{E_\perp} \cdot \frac{R}{t}\right) \tag{A.26}$$

$$M_{o,3} = 1.6400 \cdot (Rt)^{3/2} \cdot \left(E_\parallel \sigma_{\perp u}\right)^{1/2} \cdot \left(1 - 0.4086 \cdot \frac{\sigma_{\perp u}}{E_\perp} \cdot \frac{R}{t}\right) \tag{A.27}$$

$$M_{o,4} = 2.4367 \cdot (Rt)^{3/2} \cdot \left(E_\parallel \sigma_{\perp u}\right)^{1/2} \cdot \left(1 - 0.9024 \cdot \frac{\sigma_{\perp u}}{E_\perp} \cdot \frac{R}{t}\right) \tag{A.28}$$

Normalising equations (A.25)-(A.28) with $A^{1.5}$ (where $A = 2\pi Rt$ is the cross-section area):

$$\frac{M_{o,1}}{A^{1.5}} = 0.1364 \cdot \left(E_\parallel \sigma_{\perp u}\right)^{1/2} \cdot \left(1 - 0.7012 \cdot \frac{\sigma_{\perp u}}{E_\perp} \cdot \phi\right) \tag{A.29}$$

$$\frac{M_{o,2}}{A^{1.5}} = 0.1114 \cdot \left(E_\parallel \sigma_{\perp u}\right)^{1/2} \cdot \left(1 - 0.4680 \cdot \frac{\sigma_{\perp u}}{E_\perp} \cdot \phi\right) \tag{A.30}$$

$$\frac{M_{o,3}}{A^{1.5}} = 0.1041 \cdot \left(E_\parallel \sigma_{\perp u}\right)^{1/2} \cdot \left(1 - 0.4086 \cdot \frac{\sigma_{\perp u}}{E_\perp} \cdot \phi\right) \tag{A.31}$$

$$\frac{M_{o,4}}{A^{1.5}} = 0.1547 \cdot \left(E_\parallel \sigma_{\perp u}\right)^{1/2} \cdot \left(1 - 0.9024 \cdot \frac{\sigma_{\perp u}}{E_\perp} \cdot \phi\right) \tag{A.32}$$

where ϕ is the shape factor (equation (1)).

Appendix B. Bamboo culm age and moisture content for the material properties adopted herein

Table B.4: Culm age and moisture content corresponding to the experimental values of Table 1

study	[11]	[13]	[14]	[21]	[30]	[31]	[32]
culm age	>3 years	4 years	2~5 years	3~6 years	N/A	N/A	2~5 years
moisture content	5.0~20.0%	9.1%	8.5~15.0%	av. 13.8%	approx. 12.0%	av. 9.1%	adjusted to 12.0%

References

[1] L. Huang, G. Krigsvoll, F. Johansen, Y. Liu, X. Zhang, Carbon emission of global construction sector, Renewable and Sustainable Energy Reviews 81 (2018) 1906–1916. doi:10.1016/j.rser.2017.06.001.

[2] J. A. A. Janssen, Bamboo in building structures, Ph.D. thesis, University of Eindhoven (1981).

[3] W. Wu, Q. Liu, Z. Zhu, Y. Shen, Managing bamboo for carbon sequestration, bamboo stem and bamboo shoots, Small-Scale Forestry 14 (2) (2015) 233–243. doi:10.1007/s11842-014-9284-4.

[4] W. Liese, Research on bamboo, Wood Science and Technology 21 (3) (1987) 189–209.

[5] GABC, 2020 Global status report for buildings and construction - Towards a zero-emissions, efficient and resilient buildings and construction sector, Tech. rep., UN Environment Programme (2020).

[6] ISO 22156:2021(E) Bamboo structures - Bamboo culms -Structural design, BSI standards (2021).

[7] X. Wang, H. Ren, B. Zhang, B. Fei, I. Burgert, Cell wall structure and formation of maturing fibres of moso bamboo (*Phyllostachys pubescens*) increase buckling resistance, Journal of The Royal Society Interface 9 (70) (2012) 988–996. doi:10.1098/rsif.2011.0462.

[8] P. G. Dixon, L. J. Gibson, The structure and mechanics of Moso bamboo material, Journal of The Royal Society Interface 11 (99) (2014) 20140321. doi:10.1098/rsif.2014.0321.

[9] S. Mannan, J. Paul Knox, S. Basu, Correlations between axial stiffness and microstructure of a species of bamboo, Royal Society Open Science 4 (1) (2017) 160412. doi:10.1098/rsos.160412.

[10] Y. Akinbade, K. A. Harries, C. V. Flower, I. Nettleship, C. Papadopoulos, S. Platt, Through-culm wall mechanical behaviour of bamboo, Construction and Building Materials 216 (2019) 485–495. doi:https://doi.org/10.1016/j.conbuildmat.2019.04.214.

[11] K. Chung, W. Yu, Mechanical properties of structural bamboo for bamboo scaffoldings, Engineering Structures 24 (4) (2002) 429 – 442. doi:https://doi.org/10.1016/S0141-0296(01)00110-9.

[12] R. A. Sá Ribeiro, M. G. Sá Ribeiro, I. P. Miranda, Bending strength and nondestructive evaluation of structural bamboo, Construction and Building Materials 146 (2017) 38–42. doi:https://doi.org/10.1016/j.conbuildmat.2017.04.074.

[13] R. Lorenzo, L. Mimendi, D. Yang, H. Li, T. Mouka, E. G. Dimitrakopoulos, Non-linear behaviour and failure mechanism of bamboo poles in bending, Construction and Building Materials 305 (2021) 124747. doi:https://doi.org/10.1016/j.conbuildmat.2021.124747.

[14] D. Trujillo, S. Jangra, J. M. Gibson, Flexural properties as a basis for bamboo strength grading, Proceedings of the Institution of Civil Engineers - Structures and Buildings 170 (4) (2017) 284–294. doi:10.1680/jstbu.16.00084.

[15] ISO 22157:2019(E), Bamboo Structures - Determination of physical and mechanical properties of bamboo culms- Test methods, International Organization for Standardization (2019).

[16] R. Gnanaharan, J. J. Janssen, O. A. Arce, Bending strength of guadua bamboo: comparison of different testing procedures, New Delhi: International Network of Bamboo and Rattan (1995).

[17] Nurmadina, N. Nugroho, E. T. Bahtiar, Structural grading of gigantochloa apus bamboo based on its flexural properties, Construction and Building Materials 157 (2017) 1173–1189. doi:https://doi.org/10.1016/j.conbuildmat.2017.09.170.

[18] R. Lorenzo, L. Mimendi, H. Li, D. Yang, Bimodulus bending model for bamboo poles, Construction and Building Materials 262 (2020) 120876. doi:https://doi.org/10.1016/j.conbuildmat.2020.120876.

[19] L. Tian, J. Wei, J. Hao, Q. Wang, Characterization of the flexural behavior of bamboo beams, Journal of Renewable Materials 9 (9) (2021) 1571–1597. doi:10.32604/jrm.2021.015166.

[20] U. G. Wegst, M. F. Ashby, The structural efficiency of orthotropic stalks, stems and tubes, Journal of Materials Science 42 (21) (2007) 9005–9014. doi:10.1007/s10853-007-1936-8.

[21] T. Paraskeva, G. Grigoropoulos, E. Dimitrakopoulos, Design and experimental verification of easily constructible bamboo footbridges for rural areas, Engineering Structures 143 (2017) 540 – 548. doi:https://doi.org/10.1016/j.engstruct.2017.04.044.

[22] L. G. Brazier, R. V. Southwell, On the flexure of thin cylindrical shells and other "thin" sections, Proceedings of the Royal Society of London. Series A, Containing Papers of a Mathematical and Physical Character 116 (773) (1927) 104–114. doi:10.1098/rspa.1927.0125.

[23] D. Mitch, K. A. Harries, B. Sharma, Characterization of splitting behavior of bamboo culms, Journal of Materials in Civil Engineering 22 (11) (2010) 1195–1199. doi:10.1061/(ASCE)MT.1943-5533.0000120.

[24] B. Sharma, K. A. Harries, K. Ghavami, Methods of determining transverse mechanical properties of full-culm bamboo, Construction and Building Materials 38 (2013) 627 – 637, 25th Anniversary Session for ACI 228 – Building on the Past for the Future of NDT of Concrete. doi:https://doi.org/10.1016/j.conbuildmat.2012.07.116.

[25] M. J. Richard, J. Gottron, K. A. Harries, K. Ghavami, Experimental evaluation of longitudinal splitting of bamboo flexural components, Proceedings of the Institution of Civil Engineers - Structures and Buildings 170 (4) (2017) 265–274. doi:10.1680/jstbu.16.00072.

[26] U. G. Wegst, Bending efficiency through property gradients in bamboo, palm, and wood-based composites, Journal of the Mechanical Behavior of Biomedical Materials 4 (5) (2011) 744–755. doi:https://doi.org/10.1016/j.jmbbm.2011.02.013.

[27] U. G. Wegst, H. Bai, E. Saiz, A. P. Tomsia, R. O. Ritchie, Bioinspired structural materials, Nature Materials 14 (2015) 23–36. doi:https://doi.org/10.1038/nmat4089.

[28] W. C. Young, R. D. Budynas, Roark's formulas for stress and strain, 7th Edition, McGraw-Hill, Two Penn Plaza, New York, NY 10121-2298, 2002, Ch. 9: Bending of curved beams, pp. 267–380.

[29] P. Hoogenboom, R. Spaan, Shear stiffness and maximum shear stress of tubular members, in: Proceedings of the Fifteenth International Offshore and Polar Engineering Conference, Seoul, Korea, June 19-24, 2005.

[30] R. Moran, K. Webb, K. Harries, J. J. García, Edge bearing tests to assess the influence of radial gradation on the transverse behavior of bamboo, Construction and Building Materials 131 (2017) 574 – 584. doi:https://doi.org/10.1016/j.conbuildmat.2016.11.106.

[31] T. Mouka, E. G. Dimitrakopoulos, Simulation of embedment phenomena on bamboo culms via a modified foundation modelling approach, Construction and Building Materials 275 (2021) 122048. doi:https://doi.org/10.1016/j.conbuildmat.2020.122048.

[32] R. Lorenzo, M. Godina, L. Mimendi, H. Li, Determination of the physical and mechanical properties of moso, guadua and oldhamii bamboo assisted by robotic fabrication, Journal of Wood Science 66 (1) (2020) 1–11.

[33] R. Lorenzo, L. Mimendi, M. Godina, H. Li, Digital analysis of the geometric variability of Guadua, Moso and Oldhamii bamboo, Construction and Building Materials 236 (2020) 117535. doi:https://doi.org/10.1016/j.conbuildmat.2019.117535.

[34] U. G. Wegst, Bamboo and wood in musical instruments, Annual Review of Materials Research 38 (1) (2008) 323–349. doi:10.1146/annurev.matsci.38.060407.132459.